npj | Quantum Materials

www.nature.com/npjquantmats

ARTICLE OPEN

Magnetism and in-gap states of 3*d* transition metal atoms on superconducting Re

Lucas Schneider[1], Manuel Steinbrecher[1,7], Levente Rózsa[1], Juba Bouaziz[2], Krisztián Palotás[3,4,5,6], Manuel dos Santos Dias[2], Samir Lounis[2], Jens Wiebe[1] and Roland Wiesendanger[1]

Magnetic atoms on heavy-element superconducting substrates are potential building blocks for realizing topological superconductivity in one- and two-dimensional atomic arrays. Their localized magnetic moments induce so-called Yu-Shiba-Rusinov (YSR) states inside the energy gap of the substrate. In the dilute limit, where the electronic states of the array atoms are only weakly coupled, proximity of the YSR states to the Fermi energy is essential for the formation of topological superconductivity in the band of YSR states. Here, we reveal via scanning tunnel spectroscopy and ab initio calculations of a series of 3*d* transition metal atoms (Mn, Fe, Co) adsorbed on the heavy-element superconductor Re that the increase of the Kondo coupling and sign change in magnetic anisotropy with *d*-state filling is accompanied by a shift of the YSR states through the energy gap of the substrate and a crossing of the Fermi level. The uncovered systematic trends enable the identification of the most promising candidates for the realization of topological superconductivity in arrays of similar systems.

npj Quantum Materials (2019)4:42 ; https://doi.org/10.1038/s41535-019-0179-7

INTRODUCTION

Recently, theoretical predictions and experimental indications of topological superconductivity in one-[1–15] and two-dimensional[16–20] arrays of magnetic atoms coupled to bulk superconductors have triggered renewed interest in the building blocks of such systems, i.e. single magnetic atoms coupled to bulk superconductors.[21–30] Magnetic atoms locally induce pairs of bound state resonances inside the gap of their host superconductor, known as Yu-Shiba-Rusinov (YSR) states.[31–35] One route toward topological superconductivity is to weakly couple these states in so-called YSR bands, which can be realized by a dilute array of magnetic atoms on the surface of a superconductor.[17,36] In order to enter the topologically nontrivial phase, the YSR band has to cross the Fermi level E_F. This requires the width in energy and the separation from E_F of the YSR states of the atomic building blocks to be sufficiently small.

In a classical picture, the energy position E_{YSR} of the YSR state with respect to E_F depends mainly on the *s-d*- or Kondo exchange coupling J_K of the local spin of the atom to the substrate conduction electrons.[34] For low J_K, the peaks merge with the coherence peaks at the gap edge Δ, whereas for higher J_K, they shift toward E_F and eventually cross it, commonly referred to as a quantum phase transition.[37] For even higher J_K, the in-gap states merge with the coherence peaks again. However, different effects complicate this picture calling for detailed experimental investigations. The YSR state is accompanied by the formation of the Kondo state.[23,30] Orbital effects[22,27,29] and magnetic anisotropy[25,38] can lead to multiplicity and shifts, and exchange interactions between the atoms may split or shift the YSR states.[22,39–42] It is known since the 1960s that there is a systematic trend in the evolution of the Kondo screening, which is intimately connected to J_K, within the series of 3*d* transition metal atoms doped into the bulk or onto the surface of various host metals. The Kondo temperature decreases for each unpaired *d* electron in the band, showing a minimum in the middle of the series for Mn and monotonically increasing toward lower (Cr, V, and Ti) and higher (Fe, Co, and Ni) occupations.[43–46] This systematic behavior has been ascribed to a renormalization of the Kondo coupling driven by Hund's coupling of the electrons in the successively occupied *d* orbitals.[46] Apart from the Kondo coupling, the energetic position of the YSR state is influenced by the magnetic anisotropy due to crystal field splittings.[38] Therefore, it is interesting to experimentally investigate the interplay of Kondo coupling, magnetic anisotropy, and YSR binding energy in a series of *3d* transition metal atoms adsorbed on the same superconducting substrate. Such a classification has been lacking so far, but is strongly desired regarding the design of topological superconductivity in dilute arrays of atoms on elemental superconductors.

Here, we report on a combined experimental and ab initio investigation for the heavy-element superconductor Re as a substrate ($T_c \approx 1.6$ K), for which strong indications of topological superconductivity have been previously reported in densely packed iron chains.[15] We show that the YSR state energy is shifting through the gap by increasing the 3*d*-orbital occupation going from the middle towards the right end of the 3*d* transition metal series, which correlates with a simultaneous increase in the Kondo coupling, and a transition from easy-axis to easy-plane magnetic anisotropy as revealed by spin-excitation spectroscopy. Moreover, the YSR state energy is affected by the adsorption site of the transition metal

[1]Department of Physics, University of Hamburg, D-20355 Hamburg, Germany; [2]Peter Grünberg Institute and Institute for Advanced Simulation, Forschungszentrum Jülich & JARA, D-52428 Jülich, Germany; [3]Department of Theoretical Physics, Budapest University of Technology and Economics, Budapest H-1111, Hungary; [4]Institute for Solid State Physics and Optics, Wigner Research Center for Physics, Hungarian Academy of Sciences, P. O. Box 49, Budapest H-1525, Hungary; [5]MTA-SZTE Reaction Kinetics and Surface Chemistry Research Group, University of Szeged, Szeged H-6720, Hungary; [6]Institute of Physics, Slovak Academy of Sciences, SK-84511 Bratislava, Slovakia; [7]Present address: Institute for Molecules and Materials (IMM), Radboud University, Nijmegen, The Netherlands
Correspondence: Jens Wiebe (jwiebe@physnet.uni-hamburg.de)

Received: 17 April 2019 Accepted: 8 July 2019
Published online: 08 August 2019

atom. For Fe atoms adsorbed on the hexagonal close packed (hcp) site, the YSR state overlaps with the Fermi energy, and the magnetic anisotropy favors an orientation of the spin in the surface plane. Both of these properties would favor the emergence of topological superconductivity in a dilute array made of such impurities.

RESULTS

Topographic signatures

The preparation of an atomically clean (0001) surface of a Re single crystal and subsequent successive deposition of Mn, Fe, and Co onto the cold substrate ($T < 10$ K, see Methods) usually results in a statistical distribution of atoms on the two possible hollow adsorption sites, face-centered cubic (fcc) and hcp. Figure 1a, b show constant-current images of samples where either Mn and Fe (a) or Co and Fe (b) have been deposited (see Supplementary Note 1 and Supplementary Fig. 1 for an overview image). Prior to these co-deposition experiments, all species were individually deposited and investigated, which enabled us to discern them. The atoms can be distinguished by their apparent height and their adsorption site with respect to the atomic lattice of the Re(0001) surface (Fig. 1a) determined from manipulated atom images.[47] The adsorption sites of Mn and Co have been determined by their relative positions with respect to that of Fe_{fcc} and Fe_{hcp} atoms, which have been characterized in a previous work.[15] Fe atoms have a fcc-hcp ratio of about 1:4 after deposition, appear with heights of 65 pm for Fe_{fcc} and 75 pm for Fe_{hcp}, and can be manipulated between the two sites by atom manipulation (see Methods). Mn atoms adsorb only on the fcc hollow sites, appear with a height of 90 pm and cannot be manipulated to the other site. Co atoms occupy only hcp hollow sites after deposition, but can be manipulated to the fcc site and vice versa. They appear with heights of 95 pm for Co_{fcc} and 85 pm for Co_{hcp}.

Kondo resonances and spin excitations

In Fig. 1c–g, we start by studying the spectroscopic signatures of the different species on the (0001) surface of Re in the normal metallic state in a larger energy window around E_F (see Supplementary Note 2 and Supplementary Fig. 2 for spectra measured on more atoms of each species). Superconductivity was quenched by applying an external magnetic field of $B_z = 50$ mT, higher than the critical field of bulk Re ($B_c = 20$ mT),[48] perpendicular to the surface. The Mn_{fcc} atom in Fig. 1c features a step-shaped excitation around ±1 meV on a largely flat background, which is assigned to a spin excitation as discussed below. Due to the absence of a resonance around the Fermi energy, we conclude that the Kondo energy scale k_BT_K is considerably smaller than the experimental thermal energy of 0.025 meV. On the other hand, the Co_{fcc} atom in Fig. 1f reveals a broad resonance, which indicates a relatively strong Kondo coupling of its magnetic moment (see the comment on the spatial extent of the resonances in Supplementary Note 3). Using the fit to a Frota function (dashed line, see Supplementary Note 3), a correspondingly large Kondo energy of $k_BT_K \approx 1.03$ meV can be approximated via Wilson's[49] definition $k_BT_K = 0.27\Gamma_{HWHM}$ from the half width at half maximum Γ_{HWHM}. The Co_{hcp} atom in Fig. 1g shows neither a spin excitation nor a Kondo resonance in a range of ±20 meV around E_F, signaling a vast quenching of its magnetic moment. The Fe_{fcc} (Fig. 1d) and the Fe_{hcp} atoms (Fig. 1e) reveal both kinds of features, i.e. symmetric steps around ±1 meV (see arrows) and Fano resonances at E_F, indicating an interplay of spin excitations and relatively weak Kondo coupling.[50] Comparably small Kondo energies of $k_BT_K \approx$ 0.18 meV (Fe_{fcc}) and 0.10 meV (Fe_{hcp}) are consistently estimated from the fits to Frota functions (dashed curves, see Supplementary Note 4). Note that there is an additional broad resonance for Fe_{hcp}, which points towards a second Kondo screening channel with a larger Kondo temperature comparable to that of Co_{fcc}.

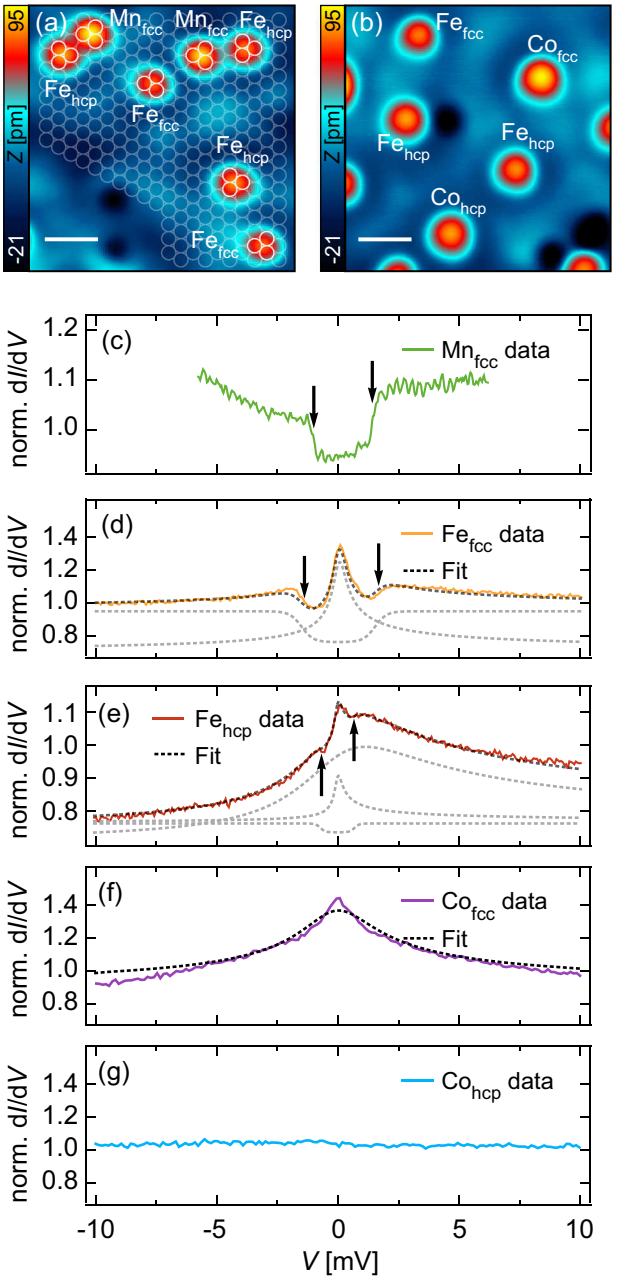

Fig. 1 Topographic and spectroscopic signatures of the 3*d* transition metal atoms. **a** Constant-current STM image of Mn and Fe atoms on different adsorption sites as indicated. The lattice of surface Re atoms determined from atom-manipulation images is overlayed (white circles). **b** Constant-current STM image of Co and Fe atoms on different adsorption sites as indicated (Scale bars in **a**, **b** have a length of 1 nm, $V = 6$ mV, $I = 200$ pA). **c–g** Tunnel spectra taken in the normal metal state of the substrate ($B_z = 50$ mT). Normalized tunnel spectra taken on (**c**) Mn_{fcc} ($V_{stab} = -6$ mV, $I_{stab} =$ 3 nA, $V_{mod} = 100$ μV), (**d**) Fe_{fcc}, (**e**) Fe_{hcp}, (**f**) Co_{fcc}, and (**g**) Co_{hcp} (V_{stab} = 20 mV, $I_{stab} = 3$ nA, $V_{mod} = 40$ μV). For Fe, the black dashed lines are fits to the sum of Frota functions, and broadened step functions at the positions indicated by the black arrows (see the different contributions indicated by gray dashed lines shifted vertically for clarity). For Co_{fcc}, the black dashed line is a fit to a Frota function

Magnetic moments and anisotropies

In Fig. 2, we investigate the magnetic-field dependence of the different spectroscopic features. The excitation observed on Mn_{fcc}, see Fig. 2a, linearly shifts as a function of B_z reminiscent of the spin

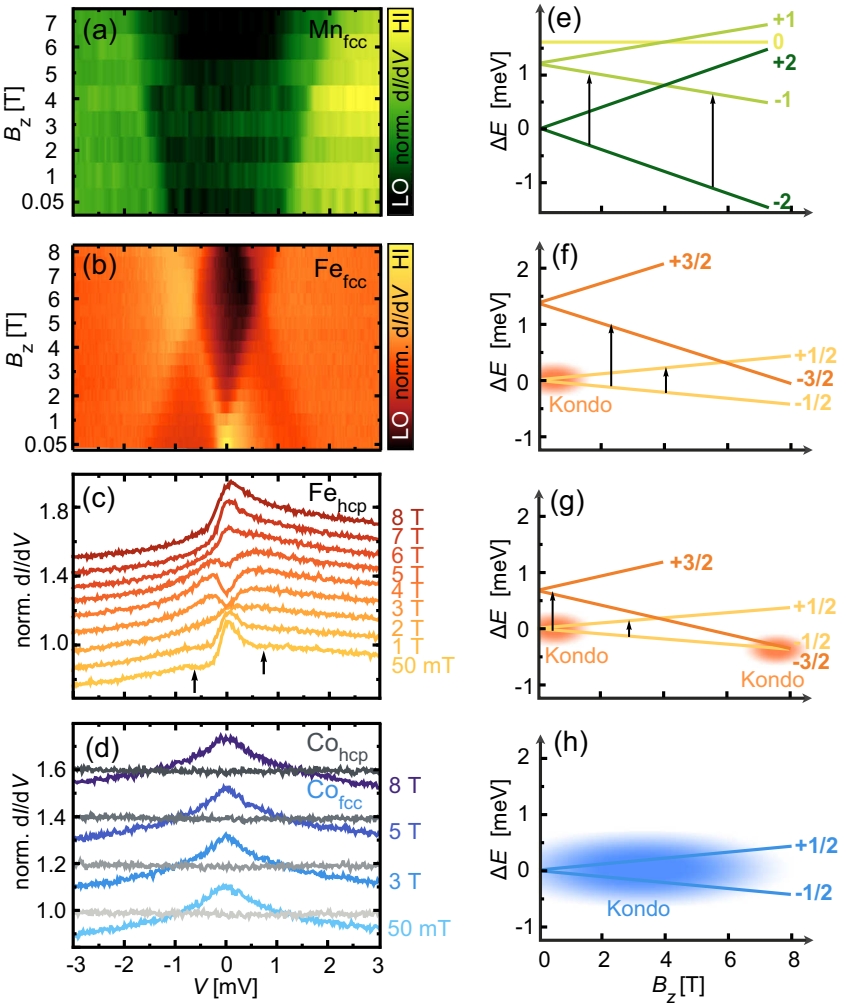

Fig. 2 Magnetic-field-dependent tunnel spectra and energy level diagrams. **a** Normalized tunnel spectra measured on Mn_{fcc} ($V_{stab} = -6$ mV, $I_{stab} = 3$ nA, $V_{mod} = 100$ μV, spectra from 0.05 to 3 T and 4 to 7 T were measured on two different atoms). **b** Normalized tunnel spectra measured on Fe_{fcc} ($V_{stab} = 3$ mV, $I_{stab} = 1$ nA, $V_{mod} = 60$ μV). **c** Normalized tunnel spectra measured on Fe_{hcp} ($V_{stab} = 3$ mV, $I_{stab} = 1$ nA, $V_{mod} = 60$ μV). **d** Normalized tunnel spectra measured on Co_{hcp} (gray) and Co_{fcc} (blue-purple, $V_{stab} = 3$ mV, $I_{stab} = 1$ nA, $V_{mod} = 60$ μV). The spectra in **c**, **d** are vertically offset for clarity. The black arrows in **c** mark the position of the supposed inelastic excitation at $B_z = 50$ mT. **e–h** Magnetic-field-dependent eigenenergies of the effective spin Hamiltonians which are consistent with the experimental data in the same row on the left, using the following parameters: (**e**) Mn_{fcc}, $S = 2$, $K = -1.56$ meV, $g = 2$; (**f**) Fe_{fcc}, $S = 3/2$, $K = +1.55$ meV, $g = 2$; (**g**) Fe_{hcp}, $S = 3/2$, $K = +0.79$ meV, $g = 1.5$; (**h**) Co_{fcc}, $S = 1/2$. The black arrows indicate the tunnel-electron-induced transitions from the ground state fulfilling the selection rules. The clouds illustrate the regions where many-body Kondo correlations can occur involving almost degenerate ground states separated by $\Delta S_z = +1$ or -1

excitation of an atom with a uniaxial out-of-plane magnetic anisotropy.[51] For Fe_{fcc}, see Fig. 2b, the resonance and spin excitation evolve into two step-like features (each above and below E_F), the former almost linearly increasing and the latter decreasing in energy with a crossing at $B_z \approx 6$ T. For $B_z \approx 11.5$ T the latter reaches E_F accompanied by the reappearance of a zero-bias resonance (see Supplementary Note 5 and Supplementary Fig. 5). This behavior is very reminiscent of the B_z evolution of the features seen for an atom with easy-plane magnetic anisotropy.[52] For Fe_{hcp}, see Fig. 2c, the behavior is qualitatively similar (see also Supplementary Fig. 4), but heavily obscured by a strongly asymmetric Fano line shape of the zero-bias resonance, the weakness of the excitation feature (arrows) and the broad background resonance. Finally, the Kondo resonance seen on the Co_{fcc}, see Fig. 2d, does not show any change up to 8 T, as expected from a strongly Kondo-coupled impurity.[53] The Co_{hcp} spectrum remains featureless in external magnetic field.

In order to further support these conclusions on the magnetic anisotropies and Kondo couplings, and to quantify these parameters, we simulate the tunnel spectroscopy data using models based on the effective spin Hamiltonian

$$\hat{H} = \frac{K}{S^2} \cdot \hat{S}_z^2 + g \cdot \mu_B \cdot B_z \cdot \hat{S}_z, \quad (1)$$

which includes a uniaxial anisotropy term with the coefficient of the magnetic anisotropy K, the spin quantum number S, and the z-component of the spin operator $\hat{S}_z$, and a Zeeman term with the atom's g-factor, the Bohr magneton μ_B, and the strength of the magnetic field applied in the z-direction perpendicular to the substrate plane B_z. The spin value S was determined by calculating the total magnetic moment of the atoms μ from ab initio electronic structure methods, and using the relation $\mu = gS\mu_B$ with the assumption $g = 2$. The geometry was optimized and the preferred adsorption sites were determined by using the Vienna Ab-initio Simulation Package (VASP, see Methods and

Table 1. Comparison of the parameters from the experiments and from the ab initio calculations

	ΔE [meV]	μ_{VASP} [μ_B]	$S = \frac{\mu_{VASP}}{2\mu_B}$	k_BT_K/Δ_{Re} experiment	$\lvert J_K\rho_F\rvert$ calc.	K_{exp}/Δ_{Re} experiment	K_{VASP}/Δ_{Re} calculated	E_{YSR}/Δ_{Re} experiment
Mn_{fcc}	−14.6	3.94	2	<0.1	0.32	−6.12 ± 0.51	−10.78	+0.90 ± 0.08
Mn_{hcp}		3.76	2	–	0.42	–	−10.86	–
Fe_{fcc}	139.5	3.08	3/2	0.71 ± 0.17	0.82	+6.08 ± 0.41	+10.27	+0.47 ± 0.15
Fe_{hcp}		2.84	3/2	0.39 ± 0.12	0.91	+3.10 ± 0.50	+6.04	+0.16 ± 0.08
Co_{fcc}	229.2	2.02	1 (1/2)	4.04 ± 0.74	1.52	–	+16.27	−0.94 ± 0.06
Co_{hcp}		1.54	1 (0)	–	1.97	–	+2.98	–

Energy difference between the adsorption sites $\Delta E = E_{fcc} - E_{hcp}$ obtained from VASP calculations, total magnetic moment of the atom μ_{VASP} obtained from VASP, and the resulting effective spin values S (note that, for Co, the experimental data suggests the values given in brackets). Experimental Kondo energy scales k_BT_K and Kondo couplings $|J_K\rho_F|$ calculated from TD-DFT within KKRJ. Uniaxial anisotropy coefficients K deduced from the fitting of the experimental spectra to the perturbation theory (Mn_{fcc} and Fe_{fcc}) and Multi-Frota (Fe_{hcp}) models using the calculated effective spins S, in comparison to the values obtained from the VASP method. YSR state energies E_{YSR} extracted from the experimental data. The energies are given with respect to the substrate energy gap of $\Delta_{Re} \approx 0.255$ meV, where meaningful. The errors in the experimental parameters have been estimated from the analysis of different atoms from each species

Supplementary Note 6).[54–56] For calculating the magnetic moments, besides the VASP package, two implementations of the Korringa–Kohn–Rostoker (KKR) Green function method based on an embedding scheme have been applied: the code developed in Budapest (KKRBp)[57,58] and the program developed in Jülich (KKRJ)[59–61] (see Methods). The VASP results are summarized in Table 1; the results of the other methods are given in Supplementary Note 7. The energy differences between the adsorption sites fit well to our experimental findings of the preferred sites. The magnetic moments of the atoms show the usual decrease from the middle toward the end of the series (Mn: ~4μ_B; Fe: ~3μ_B; Co: ~2μ_B), but with an overall reduction by 1μ_B as compared to the values of the free-standing atoms calculated from Hund's rules for 5, 4, and 3 unpaired d electrons, and a consistently smaller moment for the hcp with respect to the fcc species. The decreased magnetic moments of the atoms may be attributed to the delocalization of the d electrons due to the hybridization with the metallic substrate, which is stronger for the hcp site due to a larger relaxation towards the surface (Supplementary Note 6). The magnetic moment of Co_{hcp} decreases with respect to that of Co_{fcc} and almost vanishes within KKRBp, indicating the strong tendency towards a complete quenching of its magnetism, which can be rationalized within the Stoner picture (Supplementary Note 7). The resulting approximate values of the spin quantum number S used within the effective spin model are given in Table 1. Note, that the full physics of 3d transition metal atoms adsorbed on the metallic surface of a 5d transition metal is correctly described within the concept of a Hund's impurity,[50] where the assumption of a discrete integer or half-integer spin may be no longer valid. However, as was shown before,[50] the magnetic-field dependence of the spin excitations of a Hund's impurity are, in many cases, still modeled well by the perturbation-theory model[62] using the effective spin Hamiltonian. Therefore, we use it here in order to rationalize the excitations and zero-bias resonances, as well as to quantify the magnetic anisotropies and Kondo couplings.

The magnetic-field dependence of the simulated tunnel spectra using the perturbation-theory model[62] excellently reproduce the experimental data of Mn_{fcc} and Fe_{fcc} (see Supplementary Fig. 3 for a comparison of experimental data and simulation). The fitted values for magnetic anisotropy (K) and product of Kondo coupling with the density of states of the substrate at the Fermi level ($J_K\rho_F$) are $K = -1.56$ meV and $J_K\rho_F = -0.02$ for Mn_{fcc}, i.e. a uniaxial easy-axis anisotropy with negligible Kondo coupling, and $K = +1.55$ meV and $J_K\rho_F = -0.45$ for Fe_{fcc}, i.e. an easy-plane anisotropy and weak Kondo coupling (remaining parameters in Supplementary Note 4). The corresponding level schemes are shown in Fig. 2e and f. In particular, the zero-bias resonance and excitation step observed on the Fe_{fcc} atom can now be assigned to the Kondo state involving the degenerate $S_z = \pm 1/2$ spin levels, and degenerate spin excitations into the $S_z = \pm 3/2$ levels, respectively. They are evolving into two spin excitations (−1/2 to +1/2 and −3/2), the former increasing and the latter decreasing in energy with B_z (see arrows in Fig. 2f), which finally leads to the reappearance of the Kondo peak when the $S_z = -1/2$ and $S_z = -3/2$ levels cross around $B_z = 11.5$ T (Supplementary Note 5 and Supplementary Fig. 5). A similar easy-plane anisotropy level scheme is consistent with the experimental data of Fe_{hcp}, see Fig. 2g. However, due to the strongly asymmetric Fano line shape of the zero-bias resonance and the broad resonance of the background, the spectra cannot be fitted with the used perturbation-theory code, that does not yet include interference effects from tunneling into the hybridized d-states of the atom and into the continuum of conduction-band states of the substrate. Instead, we used a superposition of magnetic-field dependent Frota functions and steps resulting in $K = +0.79$ meV (Supplementary Note 4). For Co_{fcc} the indifference of the broad resonance to the magnetic field up to $B_z = 8$ T cannot be reconciled with the perturbation theory simulations assuming the calculated effective spin of $S = 1$. In contrast, it would be more consistent with a $S = 1/2$ impurity system in the strong Kondo-coupling regime, where the Kondo resonance is relatively insensitive to moderate magnetic fields, as shown by numerical renormalization group calculations.[53] Our experimental data therefore suggests the level scheme in Fig. 2h. Note, that this apparent discrepancy between the experiment and the ab initio calculated moment could be resolved by considering multi-channel Kondo effects of an $S = 1$ spin.[38] Finally, for Co_{hcp} the absence of any spectroscopic features around E_F is consistent with the quenching of the magnetic moment obtained from the KKRBp ab initio calculations as explained within the Stoner model.

The extracted experimental magnetic anisotropies are summarized in Table 1 together with the experimental Kondo energies. As also shown in the table, the experimentally extracted parameters are qualitatively reproduced by the magnetic anisotropy values calculated from the VASP method (see Methods) and by the Kondo couplings calculated from time-dependent density functional theory (TD-DFT) within the KKRJ method (Supplementary Note 8). Renormalization effects induced by the Kondo screening could explain the deviation of the calculated magnetic anisotropies from the experimental values.[63] The combined data reveals a systematic decrease in the magnetic moment and an increase in the Kondo coupling going from the center of the 3d transition metal series (Mn) towards the end (Co) and from fcc to hcp adsorption site. The determined Kondo energy scales thereby vary from values that are much smaller than the energy gap of the

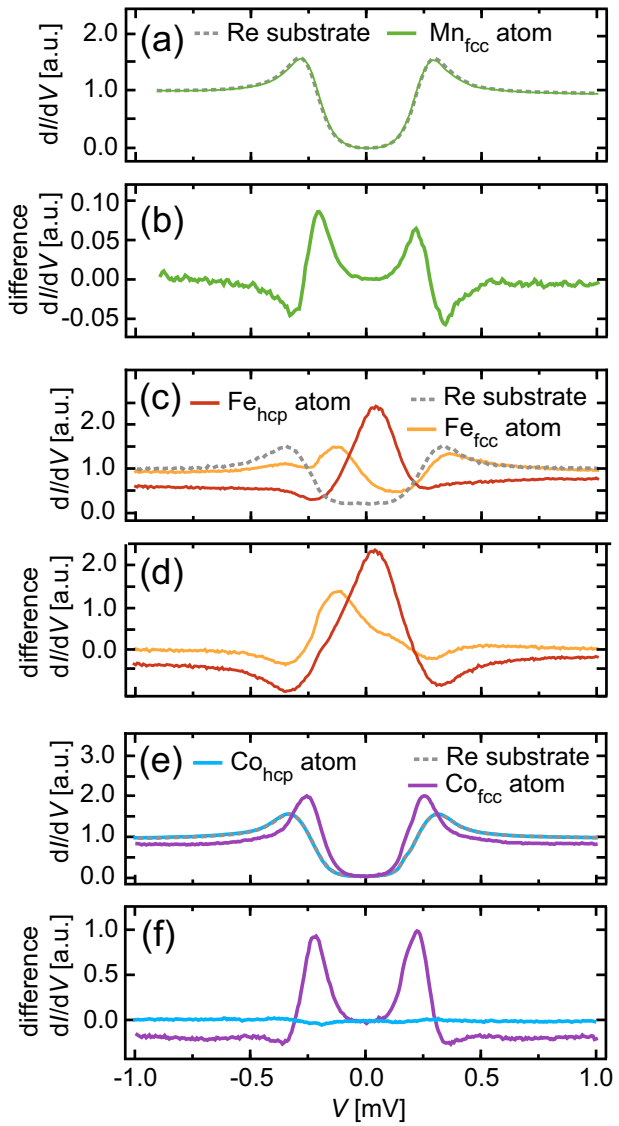

Fig. 3 Yu-Shiba-Rusinov states. **a**, **c**, **e** Raw tunnel spectra measured on (**a**) Mn_{fcc} ($V_{stab} = -1$ mV, $I_{stab} = 3$ nA, $V_{mod} = 40$ μV), (**c**) Fe_{hcp}, and Fe_{fcc} ($V_{stab} = 1$ mV, $I_{stab} = 0.2$ nA, $V_{mod} = 40$ μV), and (**e**) Co_{hcp} and Co_{fcc} atoms ($V_{stab} = 1$ mV, $I_{stab} = 0.2$ nA, $V_{mod} = 40$ μV). The dashed lines are the substrate spectra taken for each species using the same microtip. All spectra have been measured at $B_z = 0$ T. **b**, **d**, **f** Normalized tunnel spectra from each of the raw spectra in the panel above, obtained by subtraction of the respective substrate spectrum

substrate $\Delta_{Re} \approx 0.255$ meV (for Mn_{fcc}), over values comparable to Δ_{Re} (for Fe_{fcc} and Fe_{hcp}), to values that are much larger than Δ_{Re} (for Co_{fcc}). This trend is accompanied, for the particular case of adsorption on the Re(0001) substrate, by a transition in the magnetic anisotropy from easy-axis to easy-plane, where the absolute values of the magnetic anisotropy are several times larger than Δ_{Re}. In the following, we will experimentally investigate how these magnetic properties reflect in the YSR state binding energies of all species when the substrate is driven into the superconducting state ($B_z = 0$ T).

Yu-Shiba-Rusinov states

Tunnel spectroscopy performed on the Re substrate reveals the typical energy gap of Δ_{Re} with coherence peaks at the gap edges (Fig. 3a, c, e, gray dashed lines). Spectra taken on top of Mn_{fcc} (Fig. 3a, green) show a tiny shift of spectral weight from the coherence peaks into the band gap (see Supplementary Note 2 and Supplementary Fig. 2 for spectra measured on more atoms of each species). The corresponding spectroscopic features get more obvious in the normalized spectrum (Fig. 3b) exhibiting two peaks inside the gap, energetically symmetric around E_F, which we assign to the YSR states of Mn_{fcc} (see the comment on the spatial extent of the YSR states in Supplementary Note 3). The YSR states almost merge with the original coherence peaks. Considering the small Kondo coupling discussed above, we assume that the energy shift of the Mn_{fcc} YSR state from the gap edge is very small, i.e. $E_{YSR}^{Mn_{fcc}} \approx +0.23$ meV with respect to E_F. In contrast, for both types of Fe atoms, the resonances are well inside the gap, see Fig. 3c, d, which we assign to moderately bound YSR states. For the Fe_{fcc} atom the energy is around $E_{YSR}^{Fe_{fcc}} \approx +0.12$ meV. For the Fe_{hcp} atom the asymmetric shape of the tunnel spectra consists of a pair of YSR resonances at the position of roughly $E_{YSR}^{Fe_{hcp}} \approx +0.04$ meV compared to E_F, as was investigated in ref. [15] Interestingly, the narrow zero-bias features of both Fe species associated with the weak-coupling Kondo resonances shown in Fig. 1d, e are completely suppressed in the superconducting state of the Re substrate (see Supplementary Note 9 and Supplementary Fig. 7).[38] For the Co_{fcc} magnetic impurity the YSR states are again almost merging with the coherence peaks in Fig. 3e, f. Since it was found that this atom possesses the strongest Kondo coupling, we suppose that the YSR states have already crossed E_F, and are located at $E_{YSR}^{Co_{fcc}} \approx -0.24$ meV, in contrast to the positive value assigned to the Mn_{fcc} atom. Finally, the Co_{hcp} impurity does not show any signature of in-gap states, which is consistent with the full quenching of its magnetic moment.

DISCUSSION

The experimentally measured YSR binding energies are summarized in Table 1 together with the magnetic moments, anisotropies, and Kondo energies. We see that going from the center of the 3*d* transition metal series (Mn) toward the end (Co), and from fcc to hcp adsorption site, the decrease in μ and increase in k_BT_K correlates with a systematic shift of the YSR state from the coherence peak at one gap edge across E_F towards the coherence peak on the other side of the gap. The evoluton of the Kondo energies is consistent with the well-known systematics of the Kondo coupling of impurities from the 3*d* series doped into metallic hosts.[43–46] For the investigated system of atoms adsorbed on the (0001) surface of Re, the increase of k_BT_K is accompanied by a simultaneous transition of the magnetic anisotropy from out-of-plane to easy-plane. Thereby, since the absolute values of the magnetic anisotropy are large (compared to Δ_{Re}), the very nature of the sub-gap states can be affected, which complicates the phase diagram of the YSR states.[38] Therefore, we cannot disentangle the effects of Kondo coupling and magnetic anisotropy on the energetic position of the YSR states.

As we find experimentally, the magnetic state of Fe_{hcp} is closest to the situation where the YSR state just crosses E_F. This result has interesting implications considering the theoretical suggestions for the emergence of topological superconductivity in dilute arrays of weakly coupled magnetic atoms on the surface of heavy-element superconductors,[36] i.e. to choose magnetic impurities whose YSR states have a broad spectral weight at E_F. From our results, we expect that arrays of weakly coupled Fe_{hcp} atoms on Re are the most promising candidates to realize one- and two-dimensional topological superconductivity. As the Dzyaloshinskii-Moriya component of the Ruderman-Kittel-Kasuya-Yosida exchange interaction is usually strong for the heavy-element substrate,[15,64] the easy-plane magnetic anisotropy of Fe_{hcp}

facilitates the formation of non-collinear spin states in an array. This can further support topological superconductivity.

We finally expect a similar increase in the Kondo coupling for lower occupation of the 3*d* states, i.e. going from Mn over Cr and V to Ti. A comparable systematics should exist for the series of 3*d* transition metal atoms on other heavy-element superconducting substrates. Simultaneously, the magnetic anisotropy may be engineered by varying the strength of the spin-orbit coupling in the substrate. Therefore, our results enable to steer the search for topological superconductivity in the platform of dilute arrays of 3*d* transition metal atoms on heavy-element superconducting substrates.

METHODS

Experimental procedures

All measurements were performed in a home-built ultra-high-vacuum scanning tunneling microscope (STM) setup at $T = 0.3$ K with an optional magnetic field B_z of at most 12 T applied perpendicular to the sample surface.[65] We used electrochemically edged tungsten tips that were flashed to $T = 1500$ K before inserting them into the STM. The Re(0001) crystal was cleaned by Ar ion sputtering, followed by multiple cycles of O_2 annealing at $T = 1530$ K and flashing to $T = 1800$ K. Mn, Fe, and Co atoms were successively deposited keeping the substrate at $T < 10$ K. The bias-dependent differential conductance d*I*/d*V* was measured using a Lock-In amplifier by modulating the bias voltage V with $V_{mod} = 0.04$–0.20 mV at a frequency of $f_{mod} = 4142$ kHz, and at constant tip height stabilized at a bias voltage V_{stab} and tunnel current I_{stab} before opening the feedback loop for measurement. Note that the bias voltage is applied to the sample and zero bias corresponds to E_F. In order to remove any effects in the tunnel spectra measured in this way from a residual variation in the tip density of states and in order to increase the visibility of spectral features stemming from the atoms, tunnel spectra taken on the atom were normalized by division ("norm.") or subtraction ("difference") of a substrate spectrum taken with the same microtip, and are called "normalized d*I*/d*V*". Single atoms were manipulated using STM-tip-induced atom manipulation by lowering the bias voltage and increasing the setpoint current to the manipulation parameters $V = 1$ mV and $I = 100$ nA.

VASP-based calculations

During the VASP[54–56] calculations, the exchange-correlation functional was parametrized using the Perdew-Burke-Ernzerhof (PBE)[66] method within the generalized gradient (GGA) approximation. The considered system consisted of four layers of Re in hcp stacking along the (0001) direction with 7×7 atoms in each layer and a single 3*d* adatom. The in-plane lattice constant was chosen to be $a = 2.761$ Å, and the bulk interlayer distance was set to $d = 2.228$ Å. A vacuum region of minimum 9 Å was kept between the slabs in order to minimize interactions between them. The Brillouin zone was sampled by the Gamma point only because of the large supercell size. The positions of the bottom three Re layers were kept fixed during the calculations, while the Re atoms in the top layer and the adatom were allowed to relax along the direction perpendicular to the surface. It was found that allowing the atoms to also move in the plane does not make any of the adatoms switch between fcc and hcp adsorption sites, primarily because the force acting on them always points along the out-of-plane direction due to the symmetric arrangement of the neighboring Re atoms. The anisotropy coefficients K were determined from total energy differences between in-plane (x) and out-of-plane (z) orientations of the magnetic moment of the adatom, $K = E_{tot}(e_\mu \parallel e_z) - E_{tot}(e_\mu \parallel e_x)$, where e_μ, e_x, and e_z denote unit vectors along the magnetic moment direction as well as along the x and z axes. Spin-orbit coupling was included in the anisotropy calculations and $3 \times 3 \times 1$ $\boldsymbol{k}$ points were considered in the Brillouin zone integration.

KKRJ-based calculations

Within the KKR code developed in Jülich[59] the atomic sphere approximation (ASA) was used with an angular momentum cutoff of $l_{max} = 3$. Calculations based on the full-potential version of the code are presented in the Supplementary Material. The exchange and correlation potential was treated within the local density approximation (LDA) using the parametrization of Vosko, Wilk and Nusair.[67] The unit cell used for the slab calculations contained 20 Re layers in hcp stacking. The Re substrate was converged self-consistently using 40×40 $\boldsymbol{k}$ points in the full Brillouin zone. It was found that the size of the embedding cluster used to simulate the adatom was not of the same importance as recently experienced on the Pt substrate[51] for the convergence of different quantities of interest, such as the magnetic moments or the magnetic anisotropy energy. Therefore, we considered a real-space cluster containing 47 sites, including 37 Re atoms, which was built around a vacuum site located above the Re(0001) surface for the two different adsorption sites, hcp and fcc. Mn, Fe and Co impurities were then embedded self-consistently above the Re substrate. The vertical positions of the adatoms during the calculations are reported in Supplementary Note 6.

KKRBp-based calculations

Besides the VASP and KKRJ methods, we also performed electronic structure calculations using the KKR code developed in Budapest (KKRBp).[58] The potential of bulk Re was determined self-consistently as a first step. Then the surface was constructed from 8 layers of Re and four layers of empty spheres (vacuum) sandwiched between semi-infinite bulk Re and semi-infinite vacuum. The geometrical parameters were the same as in the KKRJ calculations listed in Supplementary Note 6, with the adatoms to be embedded in the vacuum layer closest to the surface. Also similarly to the KKRJ calculations, the atomic sphere approximation (ASA) was used with an angular momentum cutoff of $l_{max} = 3$. The parametrization of the exchange-correlation potential within the LDA was based on the Ceperley-Alder method.[68] The energy integration was performed on a semicircle contour containing 16 points, with up to 547 $\boldsymbol{k}$ points in the irreducible part of the Brillouin zone at the energy points close to the Fermi level. The self-consistent calculations for the adatoms were carried out by embedding a cluster of atoms in the layered system.[57] For the hcp adsorption site the cluster contained 128 atomic spheres (1 adatom, 61 Re and 66 vacuum), while 136 atomic spheres (1 adatom, 69 Re and 66 vacuum) were included for the fcc adsorption site. The direction of the exchange-correlation magnetic field $\boldsymbol{B}_{xc}$, which should be parallel to the magnetic moment in the ground state, was oriented along the out-of-plane direction for all atoms in the cluster during the self-consistent calculations.

DATA AVAILABILITY

The authors declare that the data supporting the findings of this study are available within the paper and its supplementary information files.

ACKNOWLEDGEMENTS

J.W. acknowledges fruitful discussions with Rok Žitko and Howon Kim. L.S., M.S., L.R., R.W., and J.W. acknowledge funding by the Cluster of Excellence 'Advanced Imaging of Matter' (EXC 2056 - project ID 390715994) of the Deutsche Forschungsgemeinschaft (DFG). L.S. and R.W. acknowledge funding by the ERC Advanced Grant ASTONISH (No. 338802). R.W. acknowledges funding by the ERC Advanced Grant ADMIRE (No. 786020). L.R. acknowledges funding by the Alexander von Humboldt Foundation. K.P. acknowledges support from the National Research Development and Innovation Office of Hungary project nos. K115575 and FK124100, the BME-Nanotechnology FIKP grant of EMMI, and the Slovak Academy of Sciences project no. SASPRO-1239/02/01. J.B., M.d.S.D. and S.L. acknowledge computing time granted through JARA-HPC on the supercomputer JURECA at the Forschungszentrum Jülich and funding from the European Research Council (ERC) under the European Union's Horizon 2020 research and innovation program (ERC-consolidator grant 681405 – DYNASORE).

AUTHOR CONTRIBUTIONS

L.S., M.S., R.W., and J.W. designed the experiments. L.S. and M.S. carried out the measurements. L.S. and J.W. did the analysis and the simulation of the experimental data. L.R. and K.P. performed the VASP and KKRBp-based calculations. J.B. performed the KKRJ-based and TD-DFT calculations. L.R., J.B., K.P., M.d.S.D., and S.L. analysed the ab initio simulations. L.S. and J.W. wrote the paper, to which all authors contributed via discussions and corrections.

ADDITIONAL INFORMATION

Supplementary Information accompanies the paper on the *npj Quantum Materials* website (https://doi.org/10.1038/s41535-019-0179-7).

Competing interests: The authors declare no competing interests.

REFERENCES

1. Choy, T. P., Edge, J. M., Akhmerov, A. R. & Beenakker, C. W. J. Majorana fermions emerging from magnetic nanoparticles on a superconductor without spin-orbit coupling. *Phys. Rev. B* **84**, 195442 (2011).
2. Martin, I. & Morpurgo, A. F. Majorana fermions in superconducting helical magnets. *Phys. Rev. B* **85**, 144505 (2012).
3. Braunecker, B. & Simon, P. Interplay between classical magnetic moments and superconductivity in quantum one-dimensional conductors: toward a self-sustained topological majorana phase. *Phys. Rev. Lett.* **111**, 147202 (2013).
4. Klinovaja, J., Stano, P., Yazdani, A. & Loss, D. Topological superconductivity and Majorana fermions in RKKY systems. *Phys. Rev. Lett.* **111**, 186805 (2013).
5. Nadj-Perge, S., Drozdov, I. K., Bernevig, B. A. & Yazdani, A. Proposal for realizing Majorana fermions in chains of magnetic atoms on a superconductor. *Phys. Rev. B* **88**, 020407 (2013).
6. Pientka, F., Glazman, L. I. & von Oppen, F. Topological superconducting phase in helical Shiba chains. *Phys. Rev. B* **88**, 155420 (2013).
7. Vazifeh, M. M. & Franz, M. Self-organized topological state with Majorana fermions. *Phys. Rev. Lett.* **111**, 206802 (2013).
8. Nadj-Perge, S. et al. Observation of Majorana fermions in ferromagnetic atomic chains on a superconductor. *Science* **346**, 602–607 (2014).
9. Ruby, M. et al. End states and subgap structure in proximity-coupled chains of magnetic adatoms. *Phys. Rev. Lett.* **115**, 197204 (2015).
10. Pawlak, R. et al. Probing atomic structure and Majorana wavefunctions in mono-atomic Fe chains on superconducting Pb surface. *npj Quantum Inf.* **2**, 16035 (2016).
11. Schecter, M., Flensberg, K., Christensen, M. H., Andersen, B. M. & Paaske, J. Self-organized topological superconductivity in a Yu-Shiba-Rusinov chain. *Phys. Rev. B* **93**, 140503 (2016).
12. Ruby, M., Heinrich, B. W., Peng, Y., von Oppen, F. & Franke, K. J. Exploring a proximity-coupled Co chain on Pb(110) as a possible Majorana platform. *Nano Lett.* **17**, 4473–4477 (2017).
13. Feldman, B. E. et al. High-resolution studies of the Majorana atomic chain platform. *Nat. Phys.* **13**, 286–291 (2017).
14. Jeon, S. et al. Distinguishing a Majorana zero mode using spin-resolved measurements. *Science* **358**, 772–776 (2017).
15. Kim, H. et al. Toward tailoring Majorana bound states in artificially constructed magnetic atom chains on elemental superconductors. *Sci. Adv.* **4**, eaar5251 (2018).
16. Röntynen, J. & Ojanen, T. Topological superconductivity and high Chern numbers in 2D ferromagnetic Shiba lattices. *Phys. Rev. Lett.* **114**, 236803 (2015).
17. Li, J. et al. Two-dimensional chiral topological superconductivity in Shiba lattices. *Nat. Commun.* **7**, 12297 (2016).
18. Rachel, S., Mascot, E., Cocklin, S., Vojta, M. & Morr, D. K. Quantized charge transport in chiral Majorana edge modes. *Phys. Rev. B* **96**, 205131 (2017).
19. Ménard, G. C. et al. Two-dimensional topological superconductivity in Pb/Co/Si (111). *Nat. Commun.* **8**, 2040 (2017).
20. Palacio-Morales, A. et al. Atomic-scale interface engineering of Majorana edge modes in a 2D magnet-superconductor hybrid system. Preprint at https://arxiv.org/ftp/arxiv/papers/1809/1809.04503.pdf (2018).
21. Yazdani, A., Jones, B. A., Lutz, C. P., Crommie, M. F. & Eigler, D. M. Probing the local effects of magnetic impurities on superconductivity. *Science* **275**, 1767–1770 (1997).
22. Ji, S. H. et al. High-resolution scanning tunneling spectroscopy of magnetic impurity induced bound states in the superconducting gap of Pb thin films. *Phys. Rev. Lett.* **100**, 226801 (2008).
23. Franke, K. J., Schulze, G. & Pascual, J. I. Competition of superconducting phenomena and Kondo screening at the nanoscale. *Science* **332**, 940–944 (2011).
24. Bauer, J., Pascual, J. I. & Franke, K. J. Microscopic resolution of the interplay of Kondo screening and superconducting pairing: Mn-phthalocyanine molecules adsorbed on superconducting Pb(111). *Phys. Rev. B* **87**, 075125 (2013).
25. Hatter, N., Heinrich, B. W., Ruby, M., Pascual, J. I. & Franke, K. J. Magnetic anisotropy in Shiba bound states across a quantum phase transition. *Nat. Commun.* **6**, 8988 (2015).
26. Ménard, G. C. et al. Coherent long-range magnetic bound states in a superconductor. *Nat. Phys.* **11**, 1013–1016 (2015).
27. Ruby, M., Peng, Y., von Oppen, F., Heinrich, B. W. & Franke, K. J. Orbital picture of Yu-Shiba-Rusinov multiplets. *Phys. Rev. Lett.* **117**, 186801 (2016).
28. Hatter, N., Heinrich, B. W., Rolf, D. & Franke, K. J. Scaling of Yu-Shiba-Rusinov energies in the weak-coupling Kondo regime. *Nat. Commun.* **8**, 2016 (2017).
29. Choi, D. J. et al. Mapping the orbital structure of impurity bound states in a superconductor. *Nat. Commun.* **8**, 15175 (2017).
30. Cornils, L. et al. Spin-resolved spectroscopy of the Yu-Shiba-Rusinov states of individual atoms. *Phys. Rev. Lett.* **119**, 197002 (2017).
31. Yu, L. Bound state in superconductors with paramagnetic impurities. *Acta Phys. Sin.* **21**, 75–91 (1965).
32. Shiba, H. Classical spins in superconductors. *Prog. Theor. Phys.* **40**, 435–451 (1968).
33. Rusinov, A. I. Superconductivity near a paramagnetic impurity. *Sov. Phys. Jetp.* **29**, 1101–1106 (1969).
34. Balatsky, A. V., Vekhter, I. & Zhu, J. X. Impurity-induced states in conventional and unconventional superconductors. *Rev. Mod. Phys.* **78**, 373–433 (2006).
35. Flatté, M. E. & Byers, J. M. Local electronic structure of a single magnetic impurity in a superconductor. *Phys. Rev. Lett.* **78**, 3761–3764 (1997).
36. Pientka, F., Peng, Y., Glazman, L. & von Oppen, F. Topological superconducting phase and Majorana bound states in Shiba chains. *Phys. Scr.* **T164**, 014008 (2015).
37. Farinacci, L. et al. Tuning the coupling of an individual magnetic impurity to a superconductor: Quantum phase transition and transport. *Phys. Rev. Lett.* **121**, 196803 (2018).
38. Žitko, R., Bodensiek, O. & Pruschke, T. Effects of magnetic anisotropy on the subgap excitations induced by quantum impurities in a superconducting host. *Phys. Rev. B* **83**, 054512 (2011).
39. Choi, D. J. et al. Influence of magnetic ordering between Cr adatoms on the Yu-Shiba-Rusinov states of the β-Bi_2Pd superconductor. *Phys. Rev. Lett.* **120**, 167001 (2018).
40. Ruby, M., Heinrich, B. W., Peng, Y., von Oppen, F. & Franke, K. J. Wave-function hybridization in Yu-Shiba-Rusinov dimers. *Phys. Rev. Lett.* **120**, 156803 (2018).
41. Kezilebieke, S., Dvorak, M., Ojanen, T. & Liljeroth, P. Coupled Yu-Shiba-Rusinov states in molecular dimers on $NbSe_2$. *Nano Lett.* **18**, 2311–2315 (2018).
42. Kamlapure, A., Cornils, L., Wiebe, J. & Wiesendanger, R. Engineering the spin couplings in atomically crafted spin chains on an elemental superconductor. *Nat. Commun.* **9**, 3253 (2018).
43. Daybell, M. D. & Steyert, W. A. Localized magnetic impurity states in metals: Some experimental relationships. *Rev. Mod. Phys.* **40**, 380–389 (1968).
44. Gruner, G. & Zawadowski, A. Magnetic impurities in non-magnetic metals. *Rep. Prog. Phys.* **37**, 1497–1583 (1974).
45. Jamneala, T., Madhavan, V., Chen, W. & Crommie, M. Scanning tunneling spectroscopy of transition-metal impurities at the surface of gold. *Phys. Rev. B* **61**, 9990 (2000).
46. Nevidomskyy, A. H. & Coleman, P. Kondo resonance narrowing in *d*- and *f*-electron systems. *Phys. Rev. Lett.* **103**, 147205 (2009).
47. Stroscio, J. A. & Celotta, R. J. Controlling the dynamics of a single atom in lateral atom manipulation. *Science* **306**, 242–247 (2004).
48. Roberts, B. W. Survey of superconductive materials and critical evaluation of selected properties. *J. Phys. Chem. Ref. Data.* **5**, 581–821 (1976).
49. Prüser, H. et al. Long-range Kondo signature of a single magnetic impurity. *Nat. Phys.* **7**, 203–206 (2011).
50. Khajetoorians, A. A. et al. Tuning emergent magnetism in a Hund's impurity. *Nat. Nanotechnol.* **10**, 958–964 (2015).
51. Khajetoorians, A. A. et al. Spin excitations of individual Fe atoms on Pt(111): Impact of the site-dependent giant substrate polarization. *Phys. Rev. Lett.* **111**, 157204 (2013).
52. Otte, A. F. et al. The role of magnetic anisotropy in the Kondo effect. *Nat. Phys.* **4**, 847–850 (2008).
53. Costi, T. A. Kondo effect in a magnetic field and the magnetoresistivity of Kondo alloys. *Phys. Rev. Lett.* **85**, 1504–1507 (2000).
54. Kresse, G. & Furthmüller, J. Efficient iterative schemes for ab initio total-energy calculations using a plane-wave basis set. *Phys. Rev. B* **54**, 11169 (1996).
55. Kresse, G. & Furthmüller, J. Efficiency of ab-initio total energy calculations for metals and semiconductors using a plane-wave basis set. *Comput. Mater. Sci.* **6**, 15–50 (1996).
56. Hafner, J. Ab-initio simulations of materials using VASP: density-functional theory and beyond. *J. Comput. Chem.* **29**, 2044–2078 (2008).
57. Lazarovits, B., Szunyogh, L. & Weinberger, P. Fully relativistic calculation of magnetic properties of Fe, Co, and Ni adclusters on Ag(100). *Phys. Rev. B* **65**, 104441 (2002).
58. Szunyogh, L., Újfalussy, B., Weinberger, P. & Kollár, J. Self-consistent localized KKR scheme for surfaces and interfaces. *Phys. Rev. B* **49**, 2721–2729 (1994).
59. Papanikolaou, N., Zeller, R. & Dederichs, P. H. Conceptual improvements of the KKR method. *J. Phys. Condens. Matter* **14**, 2799–2823 (2002).
60. dos Santos Dias, M., Schweflinghaus, B., Blügel, S. & Lounis, S. Relativistic dynamical spin excitations of magnetic adatoms. *Phys. Rev. B* **91**, 075405 (2015).
61. Lounis, S., Costa, A. T., Muniz, R. B. & Mills, D. L. Dynamical magnetic excitations of nanostructures from first principles. *Phys. Rev. Lett.* **105**, 187205 (2010).
62. Ternes, M. Spin excitations and correlations in scanning tunneling spectroscopy. *New J. Phys.* **17**, 63016 (2015).
63. Oberg, J. C. et al. Control of single-spin magnetic anisotropy by exchange coupling. *Nat. Nanotech.* **9**, 64–68 (2014).

64. Steinbrecher, M. et al. Non-collinear spin states in bottom-up fabricated atomic chains. *Nat. Commun.* **9**, 2853 (2018).
65. Wiebe, J. et al. A 300 mK ultra-high vacuum scanning tunneling microscope for spin-resolved spectroscopy at high energy resolution. *Rev. Sci. Instrum.* **75**, 4871–4879 (2004).
66. Perdew, J. P., Burke, K. & Ernzerhof, M. Generalized gradient approximation made simple. *Phys. Rev. Lett.* **77**, 3865–3868 (1996).
67. Vosko, S. H., Wilk, L. & Nusair, M. Accurate spin-dependent electron liquid correlation energies for local spin density calculations: a critical analysis. *Canad. J. Phys.* **58**, 1200–1211 (1980).
68. Ceperley, D. M. & Alder, B. J. Ground state of the electron gas by a stochastic method. *Phys. Rev. Lett.* **45**, 566–569 (1980).